J. Astrophys. Astr. (1994) **15,** 387–414

Radio Synthesis Imaging of Anisotropic Angular Broadening in the Solar Wind

K. R. Anantharamaiah *Raman Research Institute, Bangalore 560 080, India.*
Pradeep Gothoskar *National Center for Radio Astrophysics, Poona University Campus, Ganeshkhind, Pune 430 001, India*
T. J. Cornwell *National Radio Astronomy Observatory, Very Large Array, Socorro, NM 87801, USA.*

Received 1994 May 24; accepted 1994 September 12

Abstract. We present Very Large Array observations at wavelengths of 2, 3.5, 6, and 20 cm, of angular broadening of radio sources due to the solar wind in the region 2–16 solar radii. Angular broadening is anisotropic with axial ratios in the range 2–16. Larger axial ratios are observed preferentially at smaller solar distances. Assuming that anisotropy is due to scattering blobs elongated along magnetic field lines, the distribution of position angles of the elliptically broadened images indicates that the field lines are non-radial even at the largest heliocentric distances observed here. At $5R_{\odot}$, the major axis scattering angle is ~ 0.7″ at λ= 6 cm and it varies with heliocentric distance as $R^{-1.6}$. The level of turbulence, characterized by the wave structure function at a scale of 10 km along the major axis, normalized to λ = 20 cm, has a value 20 ± 7 at $5R_{\odot}$ and varies with heliocentric distance as R^{-3}. Comparison with earlier results suggest that the level of turbulence is higher during solar maximum. Assuming a power-law spectrum of electron density fluctuations, the fitted spectral exponents have values in the range 2.8–3.4 for scale sizes between 2–35 km. The data suggests temporal fluctuations (of up to 10%) in the spectral exponent on a time scale of a few tens of minutes. The observed structure functions at different solar distances do not show any evidence for an inner scale; the upper limits are 1 km at 2 $R_{\odot}$ and 4 km at 13 $R_{\odot}$. These upper limits are in conflict with earlier determinations and may suggest a reduced inner scale during solar maximum.

Key words: Sun: solar wind, scintillations, angular broadening—Methods: observational, radio imaging.

1. Introduction

Scattering of radio waves in an inhomogeneous medium leads to angular broadening of radio sources which can be measured using suitable interferometers. Under certain scattering conditions, the intensity of the radio source fluctuates with time giving rise to the phenomena of scintillations. Interferometric measurements of angular broadening is useful in determining several properties of the scattering medium. The mutual coherence function, which an interferometer measures, is directly related to the wave structure function of the scattering medium, which, in turn, is related to the spectrum of the density fluctuations (Coles & Harmon 1989). Any anisotropy in the scattering medium, which may be related to the orientation of the magnetic field, is directly obtained by either a radio synthesis image or a model fit to the measured visibilities. In the case of interplanetary scintillations (IPS) the intervening medium is the solar wind, which is an outflowing plasma generated near the sun and accelerated outwards to reach a velocity of ~ 400 km s $^{-1}$ at ~ 30 solar radii ($R_{\odot}$). Angular broadening of the strong radio source, Crab nebula, due to scattering in the solar wind, has been studied using simple interferometers from as early as 1952 (Machin & Smith 1952; Hewish 1955; Vitkevich 1955; Hewish 1958; Slee 1959; Hogbom 1960; Erickson 1964) and in fact predates the discovery of IPS (Hewish, Scott & Wills 1964). The first two dimensional images of angular broadening of the Crab nebula using aperture synthesis technique was obtained by Blesing & Dennison (1972) using the Culgoora radio heliograph. These early measurements, which were made at low frequencies (< 200 MHz), had already established the anisotropy in the scattering medium as also the variation of scattering angle as a function of solar distance in the range 5-60 $R_{\odot}$

The Very Large Array (VLA), which has an excellent instantaneous UV coverage with baselines up to 35 km and multiple operating wavelengths (λ = 1.3, 2, 3.5, 6, 20, 90 cm), is well suited for studying the scattering phenomena in the solar wind, especially at small solar elongations (2–20$R_{\odot}$). The mean electron density in the solar wind varies as ~ R^{-2}, where R is the distance from the Sun, and the magnitude of the scattering angle varies with observing wavelength as λ^2. It is therefore possible to tune the degree of scattering at a given elongation by choosing observing wavelengths appropriately. The high sensitivity of the VLA permits observation of even weak sources (typically < 1 Jy at 20 cm) whose lines of sight pass close to the Sun. Armstrong *et al.* (1986, 1990) were the first to use the VLA to study the angular broadening of the radio source 3C279 and obtain information on the wave structure function, anisotropy and radial dependence of scattering. Subsequently Cornwell, Anantharamaiah & Narayan (1989) used the VLA to obtain high time resolution (tens of milliseconds) images of 3C279 when its line of sight passed close to the Sun. (< 1°) and established the coherence properties of the scattered radiation. Narayan, Anantharamaiah & Cornwell (1990) used longer time-averaged images (~10 s) of 3C279 to show that refractive scintillation occurs in the solar wind and also that the area of the angular broadened image fluctuates in correlation with the total flux as predicted theoretically.

In this paper we present angular broadening observations of three radio sources using the VLA when the elongation of these sources varied between 0.5° to 4°. The motivation for these observations was to study the nature of scattering in the solar wind close to the Sun at many different position angles. At each of the observed position these data provide information on the degree of anisotropy, orientation of the major axis and level of turbulence, which are, in turn, related to the orientation of the magnetic field and the magnitude of the density fluctuations in the solar wind. The measured visibilities (correlations of the electric field) are directly related to the wave structure function of the scattering medium (Coles & Harmon 1989; Armstrong *et al.* 1990) from which we can obtain the spectrum of the density fluctuations which is assumed to have a power-law form. It may be mentioned here that for the range of elongations observed here there is no direct way of measuring either the magnetic field or the density fluctuations, since the region is too far from the Sun for solar magnetograms and too close to the Sun for space probes.

The integration time of the scatter-broadened images obtained here is typically ~ 10 minutes and therefore correspond to the so called 'ensemble-average' regime as discussed by Narayan *et al.* (1990) and Goodman & Narayan (1989). This regime is obtained when the integration time $t_{\mathrm{int}} > t_{\mathrm{ref}} = \theta_s D/V$ where θ_s is the scattering angle, D is the distance to the scattering screen (= 1 AU here) and V is the transverse velocity of the medium with respect to the observer. $\theta_s D$ (also known as the refractive scale r_{ref}) is the largest scale on the screen from which a given point in the observer plane receives the scattered radiation. Other length scales (and corresponding time scales) that come into play when scattering occurs are the Fresnel scale $r_F = \sqrt{\lambda D}$ and diffractive scale $r_{\mathrm{diff}} = \lambda/\theta_S$. r_{diff} represents the transverse scale over which the rms phase difference due to the phase changing screen is of the order 1 radian. The demarcation between weak and strong scattering regimes is at $r_{\mathrm{diff}} = r_F$. When $r_{\mathrm{diff}} < r_F$ scattering is strong and the angular broadening of the source (θ_s) is larger than the Fresnel angle ($\theta_F = r_F/D$). The behaviour of interferometric visibilities in the weak scattering regime has been discussed in detail by Cronyn (1972) and in the strong scattering regime by Narayan & Goodman (1989) and Goodman & Narayan (1989). Cornwell *et al.* (1989) have presented both theoretical and observational study of interferometric imaging in the 'snapshot' regime ($t_{\mathrm{int}} < t_{\mathrm{diff}} = r_{\mathrm{diff}}/V$) under conditions of strong scattering. A summary of the behaviour of scatter-broadened images in different regimes of integration time and scattering strength can be found in Narayan *et al.* (1990).

In the present observations which cover an elongation range of $\varepsilon = 0.5°– 4°$, we find that strong scattering occurs for $\varepsilon \leqslant 1.0°$ at $\lambda = 2$ cm, for $\varepsilon \leqslant 1.5°$ at 3.5 cm, for $\varepsilon \leqslant 2.5°$ at 6 cm and for the entire observed range of elongations at $\lambda = 20$ cm. The diffractive scales (r_{diff}) in these regions of the solar wind range from a few kilometers to several tens of kilometers at these wavelengths (which is very similar to the range of VLA baselines) and the refractive scales (r_{ref}) are about a hundred to a few thousand kilometers. The corresponding time scales are $t_{\mathrm{diff}} \sim 0.01 - 0.5$ s and $t_{\mathrm{ref}} \sim 0.5 - 50$s if we assume the solar wind velocity to be ~ 350 km s^{-1}. Notice that the length scales in. the solar wind are comparable to the baselines available in ground based radio interferometers such as the VLA and the VLBA and the time scales are comparable to typical integration times used for visibility and image measurement. Furthermore, anisotropy, which is caused by the relatively strong magnetic field (compared to interstellar conditions) in the solar wind is easily measured with these interferometers. As such, solar wind offers the right conditions for testing many predictions of scattering theories.

This paper is organized as follows. In section 2 we describe the observations and calibration of the data. Section 3 describes imaging and image analysis in which we obtain the angular size and orientation of the major and minor axes of the scatter-broadened images. The measured visibilities are analysed in section 4 in terms of the wave structure function of the scattering medium and also through least squares fit of a scattering model with parameters such as anisotropy, scattering strength, and index of the power law spectrum of density fluctuations in the medium. Finally, the derived parameters are discussed in section 5.

2. Observations

Observations were made using the A-configuration of the VLA during the period 2–6 November 1988. Three sources, 1430–155, 1437–153, and 1443–162, which are considered as VLA calibrators (i.e. they are unresolved over the range of VLA baselines) were observed each day at two or more wavelengths chosen depending on the elongation. These sources have flux densities in the range 0.50–9.0 Jy at our observing wavelengths. In Fig. 1, we show the positions of the three sources with respect to the Sun on different observing dates. Columns 1–3 of Table 1 gives the source name, date of observation, elongation and observing wavelength. Columns 3–5 of Table 2 gives the heliographic latitude, position angle of the line joining the direction of the source and the centre of the Sun measured clockwise from north and the Carrington longitude for the different dates. One of the main problems of observing close to the Sun is that the strong radio flux from the Sun's disk can enter through the side lobes of the primary beam of the antennas and corrupt the visibility measurements of the source. The problem is especially severe at longer wavelengths, where the primary beam is large and the Sun is stronger, and for short baselines, for which delay decorrelation is less. The smallest elongation where useful data could be obtained at our longest observing wavelength (λ = 20 cm) was ~ 1.3° and at the shortest wavelength (λ = 2 cm) it was ~ 0.5°.

Each source was observed for about 10 minutes in the standard VLA continuum mode with a bandwidth of 50 MHz and an integration time of 10 seconds per visibility. At each wavelength, data was recorded from both polarization channels in two intermediate frequency (IF) bands. The instrumental phase and amplitude were calibrated using observations of the source 1354–152 which was > 10° away from the Sun. The amplitude scale was set by observing the source 3C286.

The three sources were again observed on 6 January 1989 when they were > 40° away from the Sun to determine their intrinsic structure. Two of the sources (1430–155 and 1443–162) were found to be point-like and completely unresolved at all wavelengths over the VLA baselines in the A-configuration. However, the third source 1437-153 was found to be a radio galaxy with a strong core and two weak and

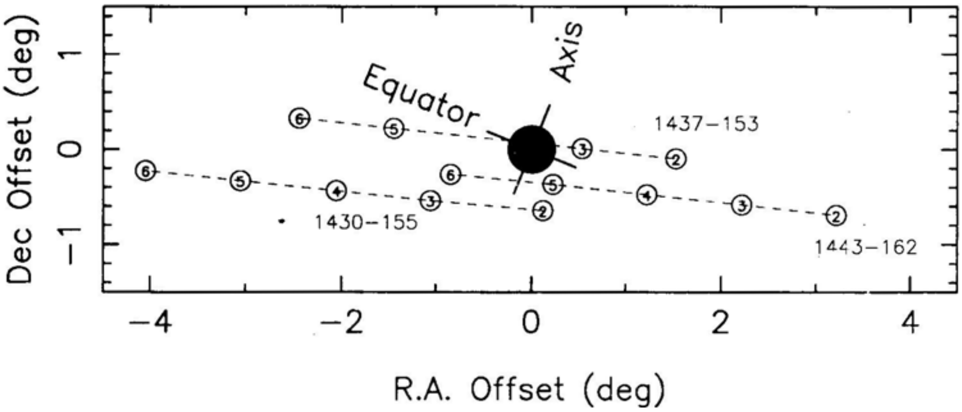

Figure 1. Position of the three observed sources with respect to the Sun on different dates. The number at each position indicates the date of observation in November 1988.

Table 1. Parameters from scatter broadened images.

Date source (1)	ϵ (°) (2)	λ (cm) (3)	Flux (Jy) (4)	θ_{maj} ($''$) (5)	θ_{min} ($''$) (6)	PA (°) (7)	ρ (8)
2 Nov.88	0.66	3.5	0.70	0.163(3)	0.06(1)	82(2)	2.8(5)
1430-155		6	0.62	0.44(1)	0.07(x)	87(9)	6.0(26)
2 Nov.88	1.53	3.5	0.82	0.088(2)	0.031(7)	11(1)	2.8(6)
1437-153		6	0.71	0.297(5)	0.105(5)	17(1)	2.8(1)
2 Nov.88	3.29	3.5	0.62	0.032(1)	0.018(1)	33(2)	1.8(1)
1443-162		6	0.57	0.08(1)	0.04(1)	34(4)	2.0(6)
		20	0.44	1.07(1)	0.39(1)	27(1)	2.7(1)
3 Nov.88	1.19	2	0.74	0.064(1)	0.017(2)	166(1)	3.8(5)
1430-155		3.5	1.04	0.125(1)	0.051(1)	154(1)	2.5(1)
		6	0.75	0.60 (1)	0.18(1)	161(1)	3.3(2)
3 Nov.88	0.54	2	0.76	0.285(7)	0.08(1)	14(1)	3.6(5)
1437-153		3.5	0.64	1.049(1)	0.29(1)	16(1)	3.6(1)
3 Nov.88	2.29	3.5	0.66	0.06(1)	0.025(5)	38(2)	2.4(6)
1443-162		6	0.52	0.205(5)	0.117(5)	23(2)	1.8(1)
		20	0.28	3.6(1)	2.18(4)	17(2)	1.7(1)
4 Nov.88	2.10	6	0.88	0.308(3)	0.08(1)	177(1)	3.7(5)
1430-155		20	0.26	4.26(3)	0.78(1)	179(1)	5.5(1)
4 Nov.88	1.31	3.5	0.61	0.16(1)	0.02(1)	38(x)	6.7(34)
1443-162		6	0.50	0.64(1)	0.16(1)	35(1)	3.9(3)
		20	0.25	9(1)	3(.5)	36(3)	2.9(6)
5 Nov.88	3.07	3.5	0.85	0.042(1)	0.022(1)	1(1)	1.9(1)
1430-155		6	0.88	0.12(1)	0.05(1)	7(2)	2.7(6)
		20	0.33	1.29(1)	0.29(1)	5(1)	4.5(2)
5 Nov.88	1.46	2	0.86	0.096(1)	0.018(5)	23(2)	5.3(15)
1437-153		3.5	0.77	0.35(1)	0.05(1)	24(1)	6.9(14)
		6	0.60	1.43(1)	0.16(1)	22(1)	8.9(6)
		20	0.39	10(1)	3.8(1)	21(3)	2.6(3)
5 Nov.88	0.43	2	0.32	0.79(1)	0.23(1)	47(1)	3.5(2)
1443-162							

Table 1. (continued).

Date source (1)	ϵ (°) (2)	λ (cm) (3)	Flux (Jy) (4)	θ_{maj} ('') (5)	θ_{min} ('') (6)	PA (°) (7)	ρ (8)
6 Nov.88	4.06	6	0.89	0.074(3)	0.016(4)	1(1)	4.6(12)
1430-155		20	0.38	0.67(3)	0.20(1)	14(1)	3.4(2)
6 Nov.88	2.46	2	1.27	0.025(4)	0.013(5)	19(10)	1.9(8)
1437-153		6	0.71	0.18(1)	0.07(1)	17(3)	2.8(4)
		20	0.54	3.28(5)	1.2(1)	24(1)	2.7(2)
6 Nov.88	0.89	2	0.74	0.245(5)	0.02(5)	175(1)	11(3)
1443-162		3.5	0.60	0.61(1)	0.075(3)	175(1)	8.2(4)
•		6	0.35	2.73(2)	0.286(4)	175(1)	9.6(2)

Notes: (1) Numbers in parenthesis are 1σ errors and apply to the last decimal digit of the value quoted.
(2) (x) indicates that the error could not be estimated.
(3) Formal error on the flux densities (column 3) is < 0.01 Jy.

extended lobes which become stronger at longer wavelengths. Visibility data of this source on short baselines is noticeably affected by its intrinsic structure at $\lambda = 20$ cm.

3. Imaging and image analysis

Images of the scatter broadened sources were obtained from the measured visibility data using standard radio synthesis methods as implemented in the software package AIPS (Astronomical Image Processing System) developed by NRAO. A common problem in synthesis imaging with long baselines and short wavelengths is the error introduced in the measured visibility (especially its phase) due to the atmosphere. On the assumption that this error is only dependent on antenna positions, corrections can be derived using the technique of self-calibration (Cornwell & Fomalont 1989). In the present case however, care should be exercised since scintillations themselves will cause fluctuations in the measured visibility phase (and amplitude). In almost all the cases observed here, we expect stable scatter-broadened images since $t_{\rm int}$ (~ 10 minutes) is much greater than $t_{\rm ref}$ (< 0.5 minutes). It several cases, especially at shorter wavelengths, images made without the application of self-calibration showed artifacts indicative of effects due to the atmosphere. In these cases, we found that application of phase corrections obtained from self-calibration with either a point-source model or an initial model obtained from positive ‘clean components’, vastly improved the quality of the images. During self-calibration, we used a visibility averaging time $t_{\rm ave}$ of one minute which is much larger than the diffractive time scale $t_{\rm diff}$ (< < 1 s) and comparable to the refractive time scale $t_{\rm ref}$. We therefore expect that the phase variations due to diffractive scintillation to be averaged out and there would be no modification of the scatter-broadened image. Cornwell *et al.* (1989) have discussed the case when $t_{\rm ave} < t_{\rm diff}$, and show that self-calibration in this regime actually removes the angular broadening because of the spatial coherence property of the scattered radiation.

Some examples of scatter-broadened images which are well resolved in the present observations are shown in Figs. 2a and 2b. These images were obtained after applying phase-corrections from self-calibration as explained above and deconvolving the 'dirty images' (Fourier transform of the measured and corrected visibility function) using conventional 'clean' For each image in Fig. 2, the direction of the line joining the center of the image and the center of the Sun's disk is indicated. Two main results of

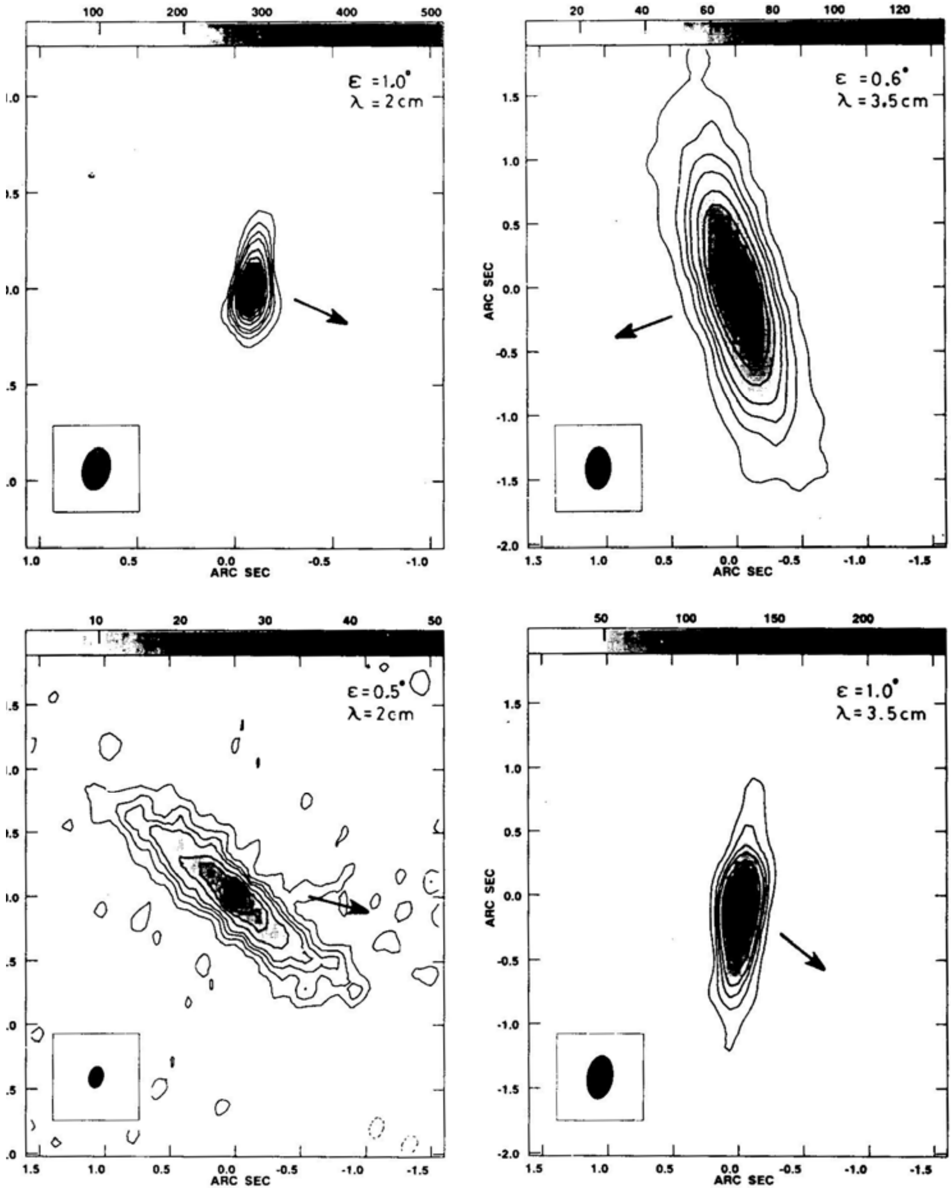

Figure 2a. Examples of scatter-broadened images at wavelengths of 2 and 3.5 cm. Elongation of the source and the wavelength of observation are indicated in each frame. Arrow indicates the direction of the Sun's centre. The contour levels are – 0.5, 0.5, 1, 1.5, 2 to 10 in steps of 1 unit where 1 unit is 43.8 mJy/beam for the top-left frame, 10.5 mJy/beam for the top-right frame, 4.1 mJy/beam for the bottom left frame and 26.7 mJy/beam for bottom-right frame. The restoring beam is shown in the bottom left corner of each image.

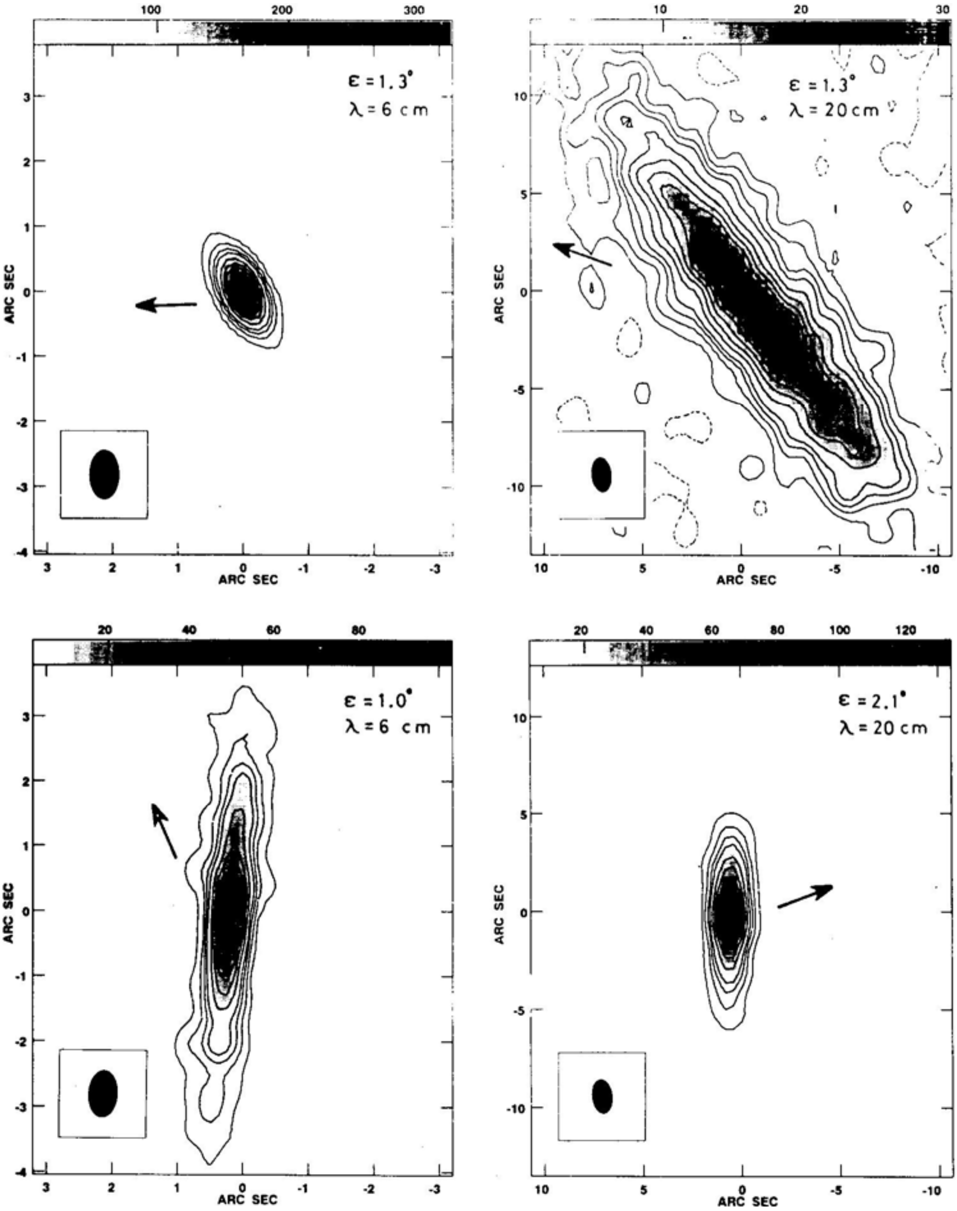

Figure 2b. Examples of scatter-broadened images at wavelengths of 6 and 20 cm. Elongation of the source and the wavelength of observation are indicated in each frame. Arrow indicates the direction of the Sun's centre. The contour levels are – 0.5, 0.5, 1, 1.5, 2 to 10 in steps of 1 unit where 1 unit is 29.1 mJy/beam for the top-left frame, 2.0 mJy/beam for the top-right frame, 8.0 mJy/beam for the bottom left frame and 11.1 mJy/beam for bottom-right frame. The restoring beam is shown at the bottom left corner of each image.

these observations are evident in Fig. 2. First, the scatter-broadening in the solar wind is highly anisotropic at small elongations in. agreement with earlier findings (Hewish 1958; Hogbom I960; Blesing & Dennison 1972; Narayan *et al.* 1989,

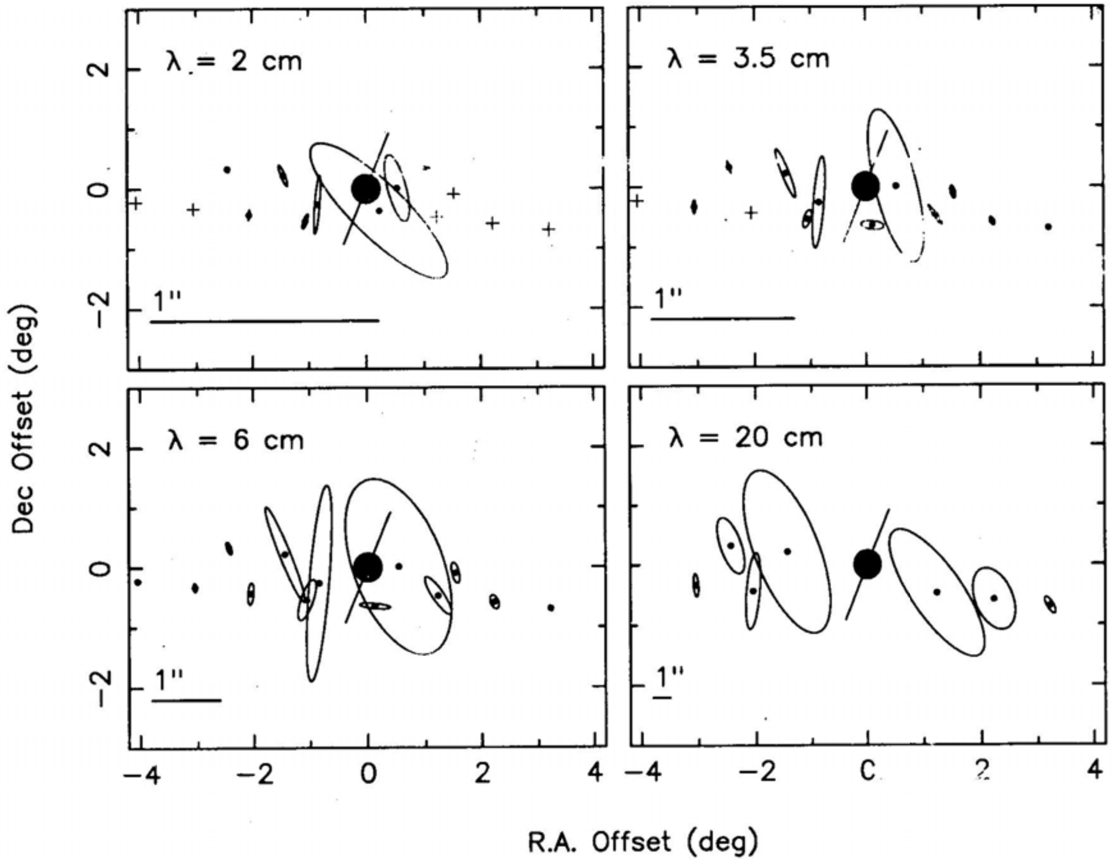

Figure 3. Schematic representation of elliptical shapes of scatter broadened images observed at four wavelengths at various distances from the Sun. The scale for the elliptical images is indicated by a 1 arcsec horizontal line in each frame. A '+' sign at the observed position indicates that the source was unresolved. The direction of the Sun's axis of rotation is indicated in each frame.

Table 2. Parameters from visibility analysis.

Date source (1)	ϵ (°) (2)	Lat. (°) (3)	ϕ_{rad} (°) (4)	Long. (°) (5)	λ (cm) (6)	Flux (Jy) (7)	x_0 (km) (8)	y_0 (km) (9)	θ(PA) (°) (10)	ρ (11)	D^{20}_{maj} (12)	D^{20}_{min} (13)	β_{fit} (14)	β_{str} (15)
2 Nov.88	0.66	−28.3	170	80.8	3.5	0.79	96(x)	27(1)	81(3)	3.6(8)	19(3)	6(5)	3.16(6)	3.16(8)
1430-155					6	0.94	59(x)	11(1)	86(4)	5.3(14)	18(2)	6(3)	2.84(8)	2.83(2)
2 Nov.88	1.53	6.9	94	80.8	3.5	0.86	210(50)	78(8)	13(x)	2.7(7)	7(6)	2.5(18)	3.18(6)	2.98(7)
1437-153					6	0.81	89(7)	26(1)	18(2)	3.5(3)	7.2(5)	1.5(5)	3.00(4)	3.27(10)
2 Nov.88	3.29	0.1	102	80.8	6	0.58	600(100)	250(25)	26(x)	2.4(5)	0.5(5)	0.3(2)	3.10(5)	3.17(11)
1443-162					20	0.48	80(7)	24(1)	28(1)	3.3(3)	0.8(1)	0.3(1)	3.12(4)	3.12(3)
3 Nov.88	1.19	−80.1	243	247.8	3.5	1.10	170(40)	52(4)	153(4)	3.3(8)	–	–	2.98(6)	–
1430-155					6	0.95	44(2)	10.5(2)	159(1)	4.2(8)	20.5(10)	5.5(5)	2.95(4)	2.98(2)
3 Nov.88	0.54	7.5	89	67.8	2	0.93	27(3)	7(.5)	13(2)	4.2(6)	370(49)	77(16)	3.22(8)	3.14(2)
1437-153					3.5	1.13	8(1)	2(.1)	15(2)	4.2(6)	305(52)	93(8)	2.98(4)	2.98(1)
3 Nov.88	2.29	−1.8	105	67.8	3.5	0.69	344(75)	159(15)	31(x)	2.2(5)	5(3)	1.4(13)	2.96(4)	2.96(18)
1443-162					6	0.58	110(8)	55(4)	24(4)	2.0(2)	4.5(6)	2.6(5)	2.90(4)	2.97(3)
					20	0.61	5(.5)	3(.2)	10(5)	1.7(2)	5.0(7)	3.3(2)	2.82(4)	2.87(2)
4 Nov.88	2.10	−31.3	258	234.6	6	0.93	190(4)	29(1)	177(2)	6.5(3)	5.8(9)	0.7(6)	3.24(4)	3.32(6)
1430-155					20	0.48	27(3)	4(.5)	178(1)	6.7(11)	4.2(7)	0.8(1)	3.06(8)	3.04(2)
4 Nov.88	1.31	-5.5	111	54.6	6	0.58	41(3)	9(.2)	36(1)	4.4(3)	23(2)	4(1)	3.28(6)	3.31(4)
1443-162					20	0.56	6(.6)	1.2(.1)	36(1)	5.0(7)	–	–	3.6(2)	3.32(5)

Table 2. (continued).

Date source (1)	ϵ (°) (2)	Lat. (°) (3)	ϕ_{rad} (°) (4)	Long. (°) (5)	λ (cm) (6)	Flux (Jy) (7)	x_0 (km) (8)	y_0 (km) (9)	θ(PA) (°) (10)	ρ (11)	D^{20}_{maj} (12)	D^{20}_{min} (13)	β_{fit} (14)	β_{str} (15)
5 Nov.88	3.07	–14.3	264	221.5	3.5	0.85	934(x)	350(x)	-3(x)	2.7(8)	–	–	3.2(1)	–
1430-155					6	0.88	515(100)	150(10)	9(4)	3.4(7)	0.8(3)	0.3(1)	3.18(4)	3.4(1)
					20	0.43	83(10)	19(1)	5(2)	4.4(6)	0.9(1)	0.2(1)	3.10(6)	3.21(3)
5 Nov.88	1.46	10	279	221.5	2	0.93	219(x)	27(2)	20(3)	8.1(17)	72(14)	–	3.20(8)	3.26(8)
1437-153					3.5	0.86	130(40)	11(.5)	24(1)	11(3)	56(2)	5(2)	3.32(6)	3.14(3)
					6	0.75	49(5)	3.8(.1)	22(1)	13(1)	64(13)	5(2)	3.24(6)	3.01(3)
5 Nov.88	0.43	–15.3	149	41.5	2	1.1	2.5(x)	0.7(.1)	46(4)	3.8(9)	–	560(346)	2.78(6)	3.19(9)
1443-162														
6 Nov.88	4.06	–7.7	267	208.3	20	0.4	211(52)	54(5)	11(4)	3.9(10)	0.2(1)	0.03(1)	3.2(3)	3.49(9)
1430-155														
6 Nov.88	2.46	–7.4	278	208.3	3.5	0.98	598(400)	160(130)	26(50)	3.7(39)	–	–	3.3(3)	–
1437-153					6	0.78	925(500)	243(100)	20(20)	3.8(26)	3.7(6)	1.5(4)	2.6(1)	2.78(5)
					20	0.67	24(10)	6(2)	24(10)	3.8(20)	3.1(3)	0.9(1)	2.9(3)	2.90(3)
6 Nov.88	0.89	–68.9	253	208.3	2	0.85	204(70)	9(.5)	175(1)	22(8)	–	–	3.20(8)	3.20(3)
1443-162					3.5	0.77	86(x)	5.5(.5)	175(1)	16(3)	120(15)	15(6)	3.0(1)	2.92(3)
					6	0.76	15(2)	1.3(.1)	175(1)	11(2)	123(25)	20(5)	2.76(4)	2.83(5)

Notes: (1) Numbers in parenthesis are 1σ errors and apply to the last decimal digit of the value quoted.
(2) (x) indicates that the error could not be estimated.
(3) Formal error on the flux densities (column 7) is < 0.01 Jy.
(4) Column 5 is Carrington longitude for the Carrington rotation number 1808.
(5) Columns 12 and 13 are the structure functions at $s = 10$ km scaled to $\lambda = 20$ cm.

Armstrong *et al.* 1990). We find that the axial ratios are in the range 2–16 depending on the elongation and position angle. In Fig. 3, we show schematically the elliptical shapes of the scatter-broadened images at different positions with respect to the Sun at four different wavelengths. The second result is that the orientation of the major axis deviates significantly from being normal to the radial from the Sun's center. At some positions, the deviation is in the range 50–75°.

An elliptical gaussian source was fitted (using the procedure JMFIT in AIPS) to each of the observed scatter-broadened image to obtain the angular size of its major and minor axes, the position angle and the total flux. The fitted values along with the formal 1σ errors are given in columns 4–7 of Table 1. Column 8 of Table 1 gives the anisotropy $\rho=\theta_{\text{maj}}/\theta_{\text{min}}$ obtained from the images.

4. Visibility analysis

Although the images shown in the previous section, which were obtained by Fourier transformation of the measured visibilities, provide a good visual picture of the scatter broadening and give quantitative estimates of the scattering angle and anisotropy, there are likely to be some biases. For example, if the scatter-broadened images are not gaussian in shape (as would be the case for a power-law spectrum of density fluctuations), then the fitted parameters will be biased. However it is possible to directly analyse the measured visibilities in terms of the scattering parameters. The measured visibilities are the time averaged electric field correlations between different points on the ground given by

$$V(\text{s}) = \langle E(\text{r})E^*(\text{r} + \text{s})\rangle \tag{1}$$

where s represents the baseline vector. The spatial coherence of the electric field described by the mutual coherence function is simply the normalized visibility given by

$$\Gamma(\mathbf{s}) = \frac{V(\mathbf{s})}{V(0)} \tag{2}$$

The mutual coherence function (equation 2) lends itself to straightforward interpretation in terms of the scattering properties of the medium and also the spatial spectrum of electron density fluctuations in the medium. The relevant theory is discussed by Coles & Harmon (1989) and Armstrong *et al.* (1990). Briefly, the mutual coherence `is related to the wave structure function $D(\mathbf{s}) = \langle[\phi(\mathbf{r}) - \phi(\mathbf{r}+\mathbf{s})]^2\rangle$ by

$$\Gamma(\mathbf{s}) = \exp\left[-\frac{D(\mathbf{s})}{2}\right] \tag{3}$$

(3) where φ(**r**) is the geometric phase delay on a straight line path from the source to the observer at position **r**. If the scattering medium is characterized by an electron density fluctuation spectrum of power-law form $P_{\text{Ne}}(q) \propto q^{-\beta}$ for $q_{\text{out}} < q < q_{\text{in}}$, where q is the wavenumber, then the wave structure function also has a power law form given by $D(s) \propto s^{\beta-2}$ for $2 < \beta < 4$. Furthermore, at the inner scale sin = $2\pi/q_{\text{in}}$ the structure function breaks to the form $D(\text{s}) \propto s^2$. A plot of log$D$(s) versus log(s) can

therefore be used to obtain the value of β and also the inner scale if it falls within the range of baselines covered by the observations. Note that useful measurements of the structure function can be obtained only over the range of baselines covered by the observations and only when the scatter broadened source is partially resolved by the interferometric array. Since the structure function $D(s)$ scales as λ^2, different wavelengths are effective for different range of scales in the scattering medium. Since the range of scales in our observations are fixed by the range of VLA baselines and since scattering angle increases with decreasing elongation, observations at shorter wavelengths (e.g. 2 cm) provide information at smaller elongations and those at longer wavelengths (e.g. 20 cm) are useful for larger elongations.

Application of the above to the present observations is slightly complicated due to the anisotropy in the scattering medium. Anisotropy implies that the scattering blobs are preferentially elongated in one direction, presumably along the local magnetic field lines. If we assume that the shape of the electron density fluctuation spectrum is independent of direction (i.e. index β has the same value along all directions) then $P_{\mathrm{Ne}}(q) \propto [q_x^2 + (q_y/\rho)^2]^{-\beta/2}$, where ρ is the axial ratio of the blobs and the x-axis is chosen along the direction of elongation in the plane normal to the line of sight. Note that any elongation along the z-direction is projected out. The structure function has the form $D(s) \propto [s_x^2 + (\rho s_y)^2]^{(\beta-2)/2}$. In the present observations, the baselines s are distributed in the xy plane and the orientation of the major axis varies from source to source. A plot of $D(s)$ versus s of all the data will show a lot of scatter since the scattering angle is a function of position angle due to the ellipticity of the image. However for baselines with the same orientation (e.g. baselines lying along one of the arms of the VLA), the mutual coherence function $\Gamma(\mathbf{s})$ and therefore the structure function $D(s)$ will show a simple monotonically increasing behaviour with s.

In Fig. 4, we show plots of log $D(s)$ versus log(s) from one of the observations for five sets of baselines; three corresponding to the three arms of the VLA and the other two to the baselines along the major and minor axis of the scatter-broadened image. To make these plots, the visibilities on each baseline were averaged over the duration of the observations (~ 10 minutes) and therefore correspond to ensemble average visibilities. Within the errors, the slopes of log $D(s)$ versus log(s) plots in Fig. 4, corresponding to the 5 sets of baselines, agree with each other indicating that the value of β is independent of direction. Plots, similar to Fig. 4, were made for all the 36 observations shown in Table 1. Out of these 36, 12 showed well determined structure functions with consistent slopes along the five different position angles. In the remaining 24 cases, 8 each had structure functions well determined along 4, 3, and 2 position angles. In these 24 cases, the structure function was not well determined at other position angles since the source was either resolved or unresolved on the available baselines. The average value of the spectral exponent β obtained from the slopes of log $D(s)$ vs. log(s) plots is given for each case in column 15 of Table 2.

The value of the structure function along the major and minor axis of the image, at $s = 10$ km and scaled to $\lambda = 20$ cm, are given in columns 12 and 13 of Table 2. The values obtained from observations at different frequencies are consistent within the errors. We further examined the consistency of the data obtained at different frequencies at a given elongation by making plots of log $D(s)$ vs log(s) for the same position angle. An example is shown in Fig. 5. For comparison the structure function

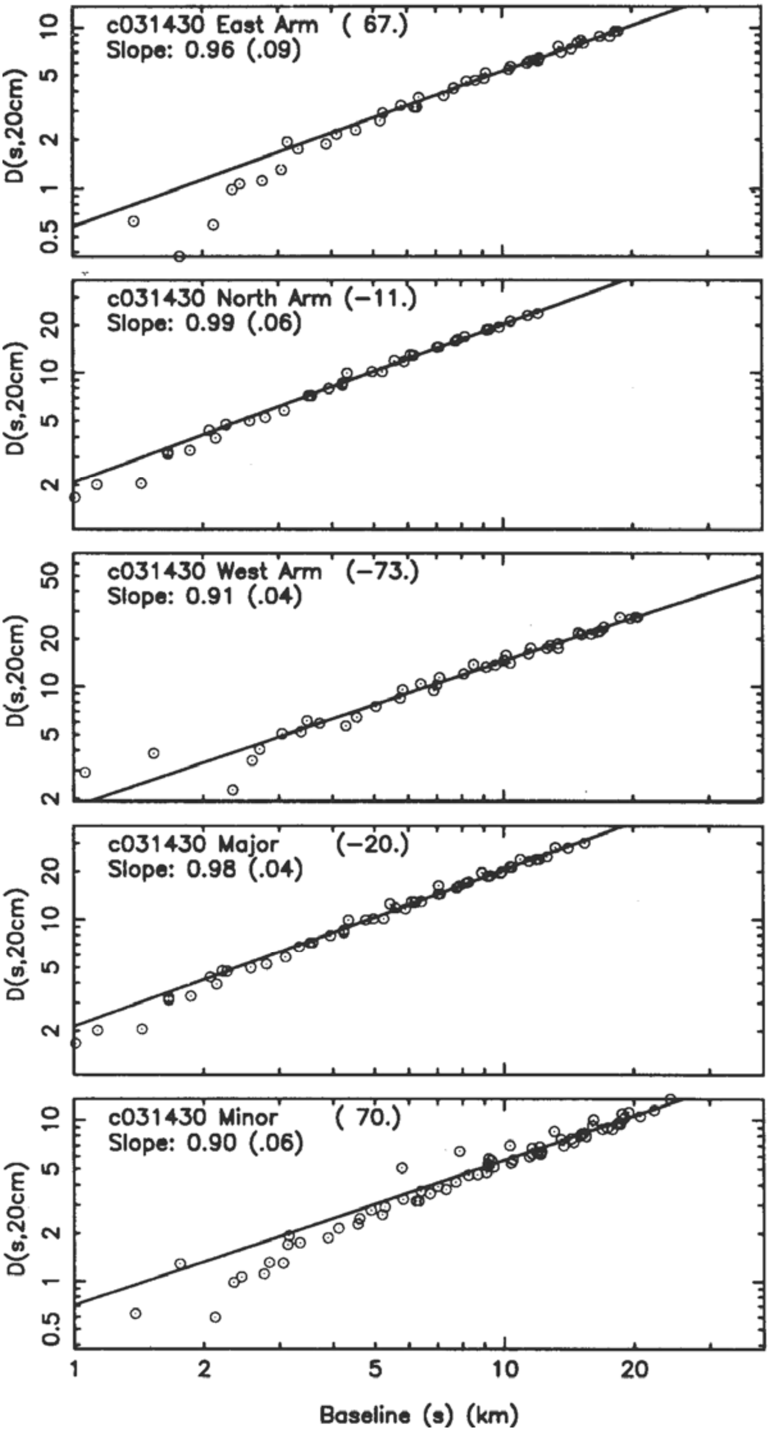

Figure 4. Structure function, scaled to λ = 20 cm, along five position angles for the source 1430155 observed at an elongation of 1.2° and λ = 6 cm. The position angles and the slope of the fitted line are given in each frame. The position angles correspond to the three arms of the VLA and the major and minor axis of the image. The slope of the structure function is equal to β-2 where β is the exponent of the power-law spectrum of electron density fluctuations defined as $P_{Ne}(q) \propto q^{-\beta}$.

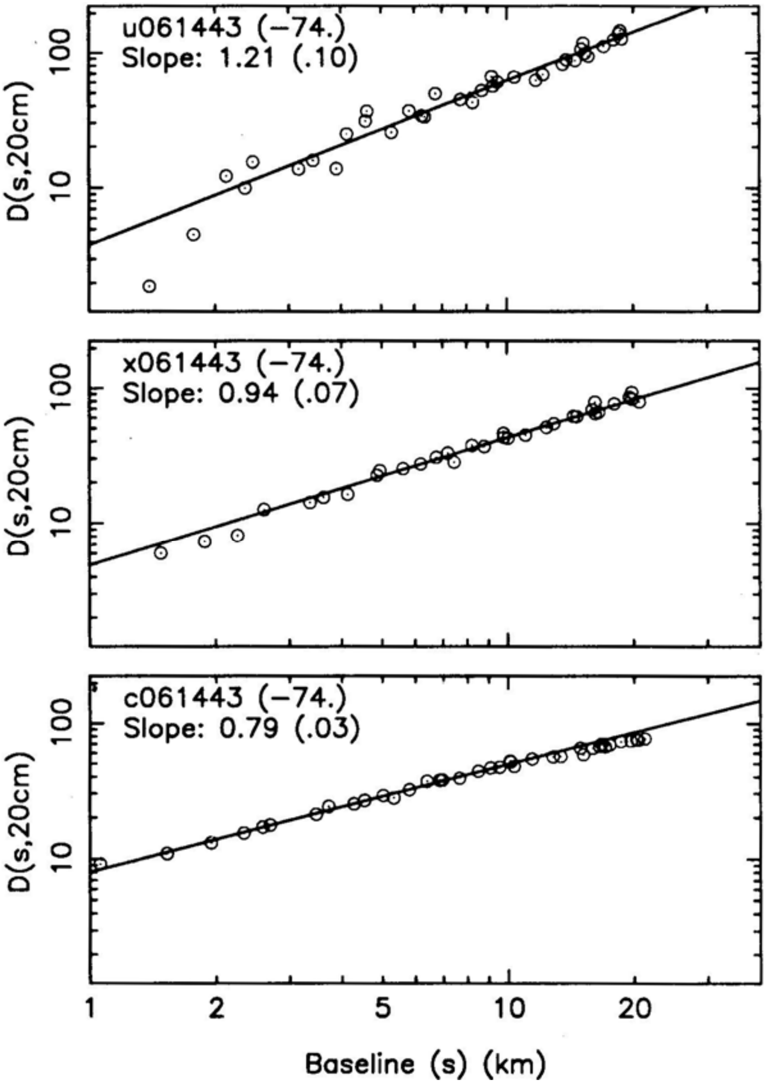

Figure 5. Structure function at 2, 3.5, and 6 cm, each scaled to λ = 20 cm, for the source 1443–162 observed at an elongation of 0.9°. The position angle is – 74° and corresponds to the east arm of the VLA. The slopes of the fitted lines and their errors are also indicated.

at each frequency has been scaled to λ = 20 cm. Fig. 5 shows that, although the magnitude of the structure function is roughly consistent at the three frequencies and follows the expected λ^2 law, the slope of the function decreases systematically with increasing wavelength. Since the range of baselines (s) over which the slopes are determined at the three frequencies are nearly the same, this variation cannot be attributed to any possible change in the spectral exponent with scale size. Presence of any inner scale within these range of baselines is also ruled out since no break is seen in the slope. We examined eleven cases for which well determined structure function (as in Fig. 5) could be obtained at more than one frequency and found no

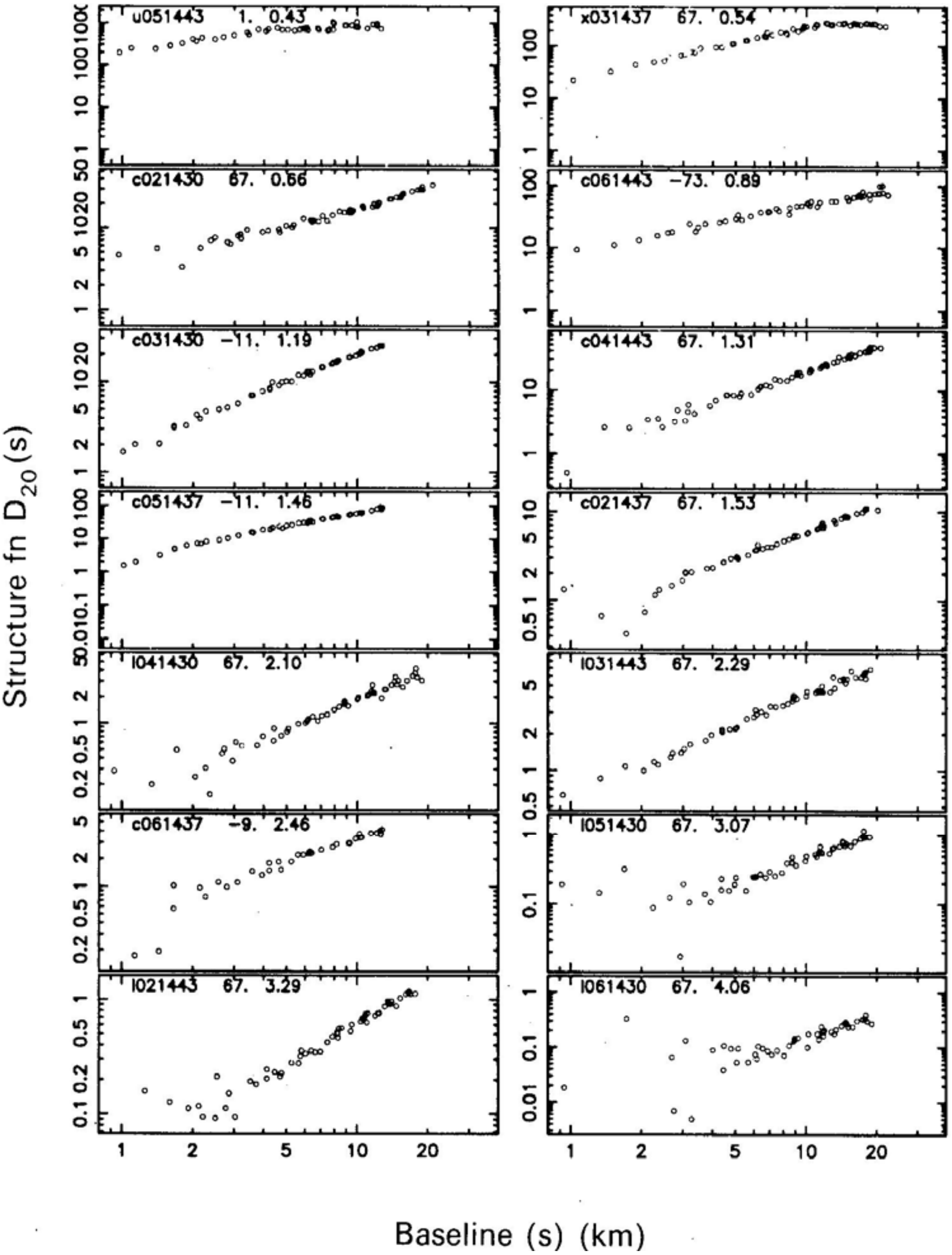

Figure 6. Structure functions, scaled to $\lambda = 20$ cm, at all the observed elongations. Wavelength of observation, date, source name, position angle of baselines and the elongation are given for each frame. For example, the top left frame is observation of the source 1443–162 at u band (i.e. $\lambda = 2$ cm) on 5th Nov. at an elongation of 0.43°. The position angle chosen is 1°. The nomenclature for the wavelengths are $x = 3.5$ cm, $c = 6$ cm and $l = 20$ cm. For each elongation, we have selected a wavelength and position angle which gives a well determined structure function over a reasonable range of baselines.

clear trend in the behaviour of β with λ; in three cases the exponent decreased with frequency as in Fig. 5, in two cases it increased, in four cases the exponent remained constant within the errors and in two cases the exponent first increased and then decreased. Given this behaviour and the fact that the observations of a given source at different frequencies were separated by 30–35 minutes, we attribute the observed variation in β to temporal fluctuations on a time scale of a few tens of minutes. Such temporal variation in β may be expected since it has been shown (Manoharan *et al.* 1994) that the spectral exponent varies with the velocity of the solar wind which fluctuates on a variety of time scales.

In Fig. 6, we present the structure function obtained at the 14 elongations where observations were made. For this plot, we have chosen, for each case, an observed frequency and a position angle for which the structure function is well determined over a reasonable range of baselines. For comparison, all the structure function values have been scaled to $\lambda = 20$ cm. In all the cases shown in Fig. 6, there is no clear indication of an inner scale at which we expect the slope of log $D(s)$ vs. log (s) to change from $\beta - 2$ to 2. In some of the cases, the structure function shows a scatter near the shortest baselines due to the source being unresolved. We estimate upper limits to the inner scale as the shortest baseline down to which log $D(s)$ shows a linear dependence on log (s) in the plots shown in Fig. 6. These limits are given in column 11 of Table 3.

In the above method of analysing the structure functions, only a part of the data is utilized in determining the value of β, since only baselines lying along a selected position angle are used. In order to use all the visibility measurements, we follow the method discussed in Narayan *et al.* (1989) which was based on a theoretical treatment of anisotropic scattering by Narayan & Hubbard (1987). In this method the ensemble average visibilities of the scatter broadened image are predicted on the basis of a five parameter model and compared with the measured visibilities. The five parameters are then optimized using a least-squares fitting algorithm. The model visibilities are given by

$$\langle V_{\mathrm{model}}(u,v) \rangle = F \times \exp[-(au_t^2 + bv_t^2)^{\gamma}] \qquad (4)$$

where F is the flux density of the source, $u_t = u \cos\theta + v \sin\theta, v_t = — u \sin\theta + \upsilon \cos\theta$, θ is the orientation of the image with respect to the u-axis, $\gamma = (\beta - 2)/2$ where β is the power-law index of electron density fluctuation spectrum and $x_0 = (1/\alpha)^{1/2}$ and $y_0 = (1/b)^{1/2}$ are the scale lengths along the major and minor axis of the scatter broadened image. These scale lengths represent the baseline at which the visibility falls to $1/e$ of its zero-spacing value, $\rho = y_o/x_o$ is the magnitude of anisotropy.

The complex visibility data on each of the 351 baselines, taken with an integration time of 10 seconds, were averaged over the duration of the observations (~ 10 minutes) and over two frequency channels and both polarizations. Self-calibration applied to the visibility data as described in the previous section ensured that the source is at the field centre and since the signal to noise ratio on each visibility measurement is sufficiently large (typically > 10), we fitted the magnitude of the 351 observed visibilities to the model given by equation 4. The five parameters (F, θ, x_o, y_o, and γ) were optimized by minimising χ^2_ν using a conjugate gradient search algorithm$_\nu$ χ^2_ν has the usual definition

$$\chi^2_\nu = \frac{\Sigma^{1/2}_{\sigma_{\mathrm{obs}}} (V_{\mathrm{model}} - V_{\mathrm{obs}})^2}{(N - n - 1)} \qquad (5)$$

where the summation is over N visibility measurements and n is the number of free parameters. $\sigma_{\rm obs}$ is the rms noise on individual visibility measurements. If the model chosen is correct and there are no systematic errors, then, χ^2_ν will approach unity when the model parameters are optimum. In order to compare the model and the observed visibilities, we define, following equation (3), a structure function at the modified scale s_m

$$D(s_m) = -2.\ln \frac{V(s_m)}{V(0)} \tag{6}$$

where s_m is a modified $U\,V$ distance given by

$$s_m = (au_t^2 + bv_t^2)^{1/2} \tag{7}$$

and $V(s_m)$ is the observed visibility on the baseline (u, v). The effect of equation (7) is to express the baseline lengths in terms of the fitted scale lengths x_0 and y_0 and the position angle θ. The structure function predicted by the model is also obtained by equation (6) by replacing the observed visibility by the model visibility $V_{\rm model}\ (s_m)$ given by equation (4). Fig. 7 shows a comparison between the observed and model structure functions (equation 6) for one of the observations. In this plot all the structure

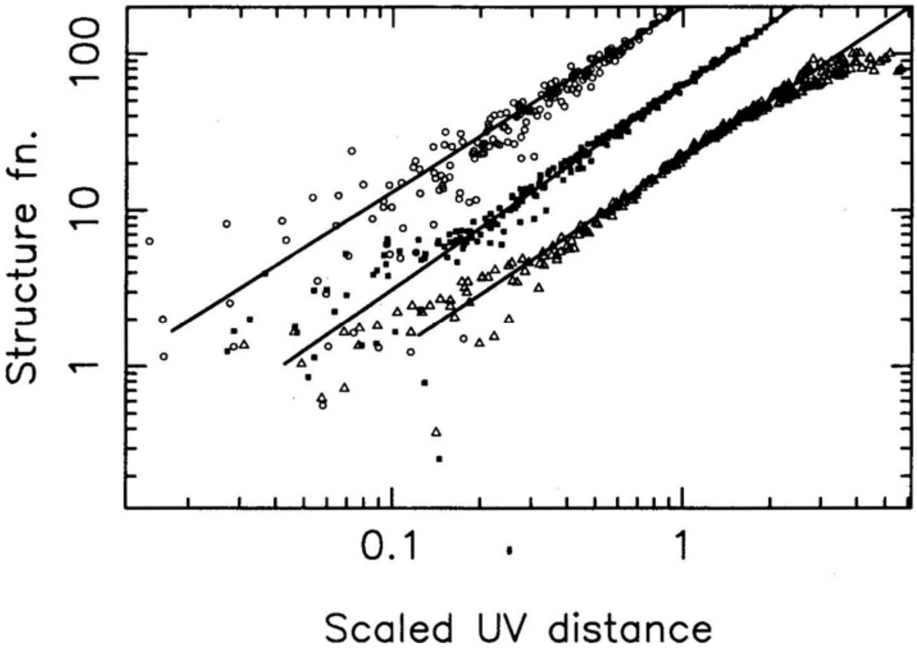

Figure 7. Comparison of observed and model visibilities for the source 1437–143 observed at an elongation of 1.5°. Open circles are observations at λ = 2 cm, solid squares are at 3.5 cm and open triangles are at 6 cm. The observed structure function (equation 6), scaled to λ = 20 cm in each case is plotted against baselines which are scaled and rotated to match the fitted scale lengths along the major and minor axis of the anisotropic image and also its orientation. The scaled baseline lengths are $(au_t^2 + bv_t^2)^{1/2}$ as used in equation (4). The fitted model given by equations (4) and (6) is plotted as a solid line.

functions have been scaled to $\lambda = 20$ cm. With the exception pf a few cases, there was good agreement (as in Fig. 7) between the model and the observed values. However, we found that the minimum value of χ_ν^2 differed from unity by a factor of 2–10 or even larger in most of the cases. We attribute this to an underestimation of σ_{obs}, which was obtained from the observed fluctuations in the visibility samples with 10 second integration by assuming that these fluctuations are independent in the four IF channels (two frequencies and two polarizations) and that the rms noise goes down

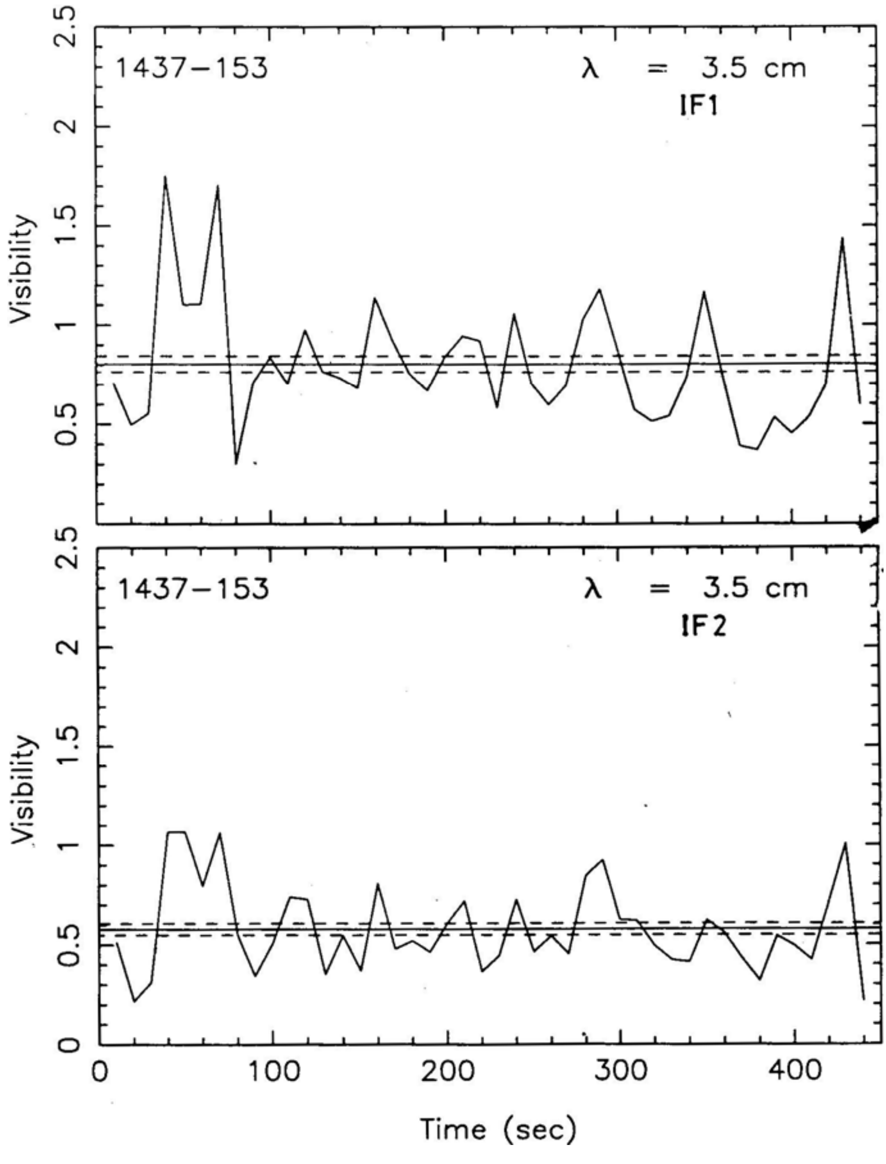

Figure 8. Time variation of the measured visibility in the two IF bands on one of the baselines (Antenna pair 21–27). The pair of dashed lines indicate the expected rms noise level for an integration time of 10 s and a bandwidth of 50 MHz which is used for the observations. The two IF bands are separated by 50 MHz.

by a factor $(1/N_{\mathrm{vis}})^{1/2}$ when N_{vis} visibility samples are averaged. Two factors have contributed to an underestimation of σ_{abs}; (i) presence of refractive scintillation with $t_{\mathrm{ref}} > 10$s, which introduces partial correlation between many 10 second samples and (ii) the decorrelation bandwidth ($c/d\theta_s^2$, where θ_s is the scattering angle and d is the length of the baseline) is much larger than the separation between the two frequency channels which results in two of the four IFs being not independent for some of the baselines. That this is indeed true can be seen in Fig. 8, where we show, the variation of visibility on one of the baselines as a function of time for two IFs. A high degree of correlation is seen between the two IFs and there are systematic fluctuations in the visibility over a time scale of several tens of seconds. Presence of refractive scintillation in the solar wind with a time scale of few minutes had been established by Narayan *et al.* (1989). A value of χ_v^2 , higher than unity when the model parameters are optimised as described above is consistent with these observations.

The best fit values of F, x_o, y_o, θ and β (= $2\gamma + 2$) along with their corresponding errors are given in columns 7–10 and 14 of Table 2. Statistical error for each parameter was obtained by using the variation of χ_v^2 with the parameter around its best fit value while keeping the other parameters fixed at their optimum values. The fitted values of β are consistent with the values derived from the structure function analysis above (i.e. slope of log $D(s)$versus log (s) plots given in column 15 of Table 2).

5. Discussion

The observations presented here sample the scattering properties of the solar wind in the region 2–16 $R_\odot$ and a range of heliographic latitudes. The parameters obtained are the magnitude of the scattering angle, the level of the structure function, the anisotropy of the scattering blobs, the orientation of the magnetic field lines, the spectral index β of the electron density fluctuation spectrum and upper limits on the inner scale of the density fluctuations. These quantities are summarized in Table 3.

5.1 *Level of turbulence*

Following Armstrong *et al.* (1990), we characterize the level of turbulence by the magnitude of the structure function at a fixed scale of 10 km normalized to $\lambda = 20$ cm. This quantity computed along the major and minor axis (denoted by D_{major} and D_{minor}) of the scattered image are given in columns 12 and 13 of Table 2 and the average values for each elongation are given in columns 7 and 8 of Table 3. Fig. 9 shows a plot of D_{major} and D_{minor} as a function of elongation on a log-log scale. The turbulence level shows a power law behaviour; the fitted slopes are -2.7 ± 0.2 for D_{major} and -3.0 ± 0.2 for D_{minor}. For a spherically symmetric solar wind having density variance proportional to the square of the mean density, the expected slope is – 3.0. From Fig. 8, the turbulence levels at 5 $R_\odot$ are $D_{\mathrm{major}} = 20 \pm 7$ and $D_{\mathrm{minor}} = 6 \pm 3$. For comparison, the corresponding values reported by Armstrong *et al.* (1990) (taken from their Fig. 4a) and ~ 7 and ~ 2 from observations in 1983 which is closer to a solar minimum. Our values are about a factor of 3 larger. This may represent the difference in the level of turbulence between solar minimum and maximum, since our observations are closer to a solar maximum. The value of the structure function at

Table 3. Parameters as a function of solar distance.

ϵ (°) (1)	$R/R_\odot$ (2)	Lat (°) (3)	ϕ_{rad} (°) (4)	θ^{6cm}_{maj} (″) (5)	ρ (6)	D^{20}_{maj} (7)	D^{20}_{min} (8)	$<\beta>$ (9)	$<PA>$ (°) (10)	s_{in} (km) (11)
0.43	1.72	−15.3	128	9.50 ±0.10†	3.8 ±0.9	–	560 ± 346	2.78 ±0.06	46 ± 4	< 1.5
0.54	2.16	7.5	106	3.55 ±0.04†	4.2 ±0.6	338 ± 35	85 ± 9	3.10 ±0.04	14 ± 2	< 1
0.66	2.64	−28.3	142	0.44 ±0.01	4.5 ±0.1	19 ± 2	6 ± 3	3.00 ±0.07	83 ± 4	< 4
0.89	3.56	−68.9	182	2.73 ±0.02	16.2 ±0.5	122 ± 15	17 ± 4	2.99 ±0.08	175 ± 1	< 1.5
1.19	4.76	−80.1	193	0.60 ±0.01	3.8 ±0.8	21 ± 1	5.5 ± 0.5	2.97 ±0.05	156 ± 3	< 2
1.31	5.24	−05.5	119	0.64 ±0.01	4.7 ±0.5	23 ± 2	4 ± 1	3.44 ±0.15	36 ± 1	< 5
1.46	5.84	10.0	291	1.43 ±0.01	10.6 ±0.2	64 ± 6	5.0 ± 1	3.25 ±0.07	22 ± 2	< 2
1.53	6.12	6.9	106	0.30 ±0.01	3.1 ±0.5	7.2 ± 0.5	2.0 ± 0.7	3.06 ±0.05	15 ± 2	< 4
2.10	8.40	−31.3	250	0.31 ±0.01	6.6 ±0.8	5.0 ± 0.6	0.8 ± 0.3	3.14 ±0.06	178 ± 2	< 4
2.29	9.16	−01.8	115	0.21 ±0.01	2.0 ±0.3	4.8 ± 1.1	2.4 ± 0.5	2.89 ±0.04	22 ± 5	< 2
2.46	9.84	−07.4	289	0.18 ±0.01	3.8 ±0.3	3.4 ± 0.4	1.2 ± 0.2	2.90 ±0.30	23 ± 32	< 3.5
3.07	12.28	−14.3	267	0.12 ±0.01	3.5 ±0.7	0.9 ± 0.3	0.3 ± 0.1	3.16 ±0.07	4 ± 3	< 6
3.29	13.16	0.1	113	0.08 ±0.01	2.9 ±0.4	0.8 ± 0.1	0.3 ± 0.1	3.11 ±0.05	27 ± 1	< 4
4.06	16.24	−07.7	274	0.07 ±0.01	3.9 ±1.0	0.2 ± 0.1	0.03 ± 0.01	3.22 ±0.07	11 ± 4	< 8

Notes: (1) †Extrapolated from higher frequency using $\theta_s \propto \lambda^{2.2}$
(2) Errors quoted are 1σ.

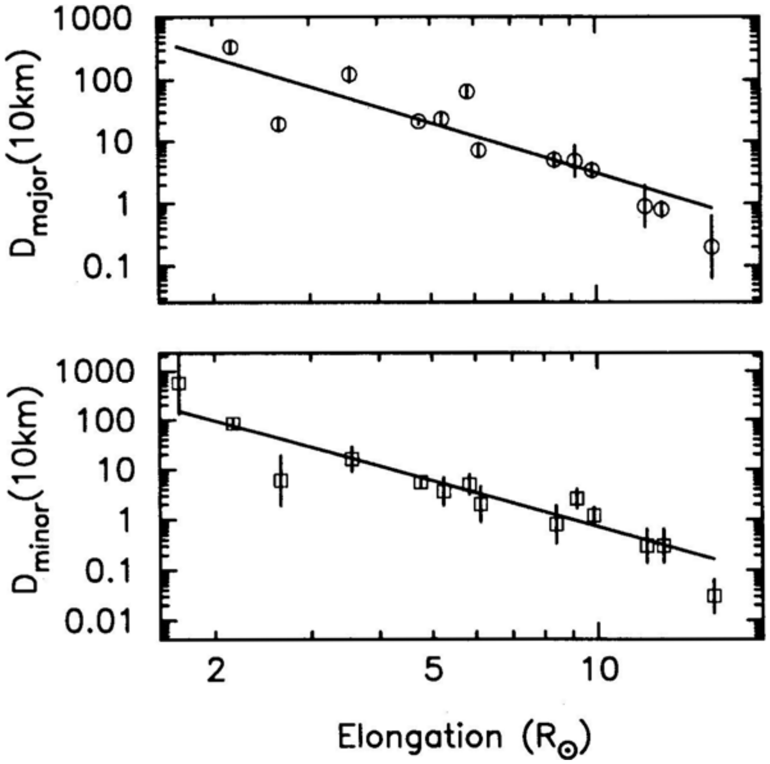

Figure 9. The variation of structure function along the major and minor axis at a scale of 10 km, normalized to $\lambda = 20$ cm, as a function of solar distance. The fitted lines have slopes of -2.7 ± 0.2 and -3.0 ± 0.2 for the top and bottom frames.

$5R_\odot$ (normalized to $\lambda = 20$ cm) obtained by Coles & Harmon (1989) (taken from their figure 1), from spectral broadening measurements in 1984, is ~ 13. Since the structure function determination from spectral broadening data requires a knowledge of the solar wind velocity, a direct comparison with D_{major} or D_{minor} obtained from visibility measurements is difficult.

5.2 *Angular broadening*

The magnitude of angular broadening (which, of course is related to the turbulence level discussed above) and its variation with solar distance is of direct interest to observers, for example, to determine the interferometric baselines required to study the scattering phenomena in the solar wind. The observed angular size along the major axis at $\lambda = 6$ cm is given in column 5 of Table 3 and plotted as function of solar distance on a log-log scale in Fig. 10a. The angular size of the major axis shows a power law dependence on solar distance R with a slope of -1.6 ± 0.1 $\theta_{\mathrm{maj}} \propto R^{-1.6}$. This type of dependence is also seen in the angular extent of the minor axis and is consistent with earlier findings (Lotova *et al.* 1989, see also compilation by Hollweg 1970 of earlier results). Angular broadening does not seem to depend on heliographic latitude. This is not surprising since these observations are made closer to the solar

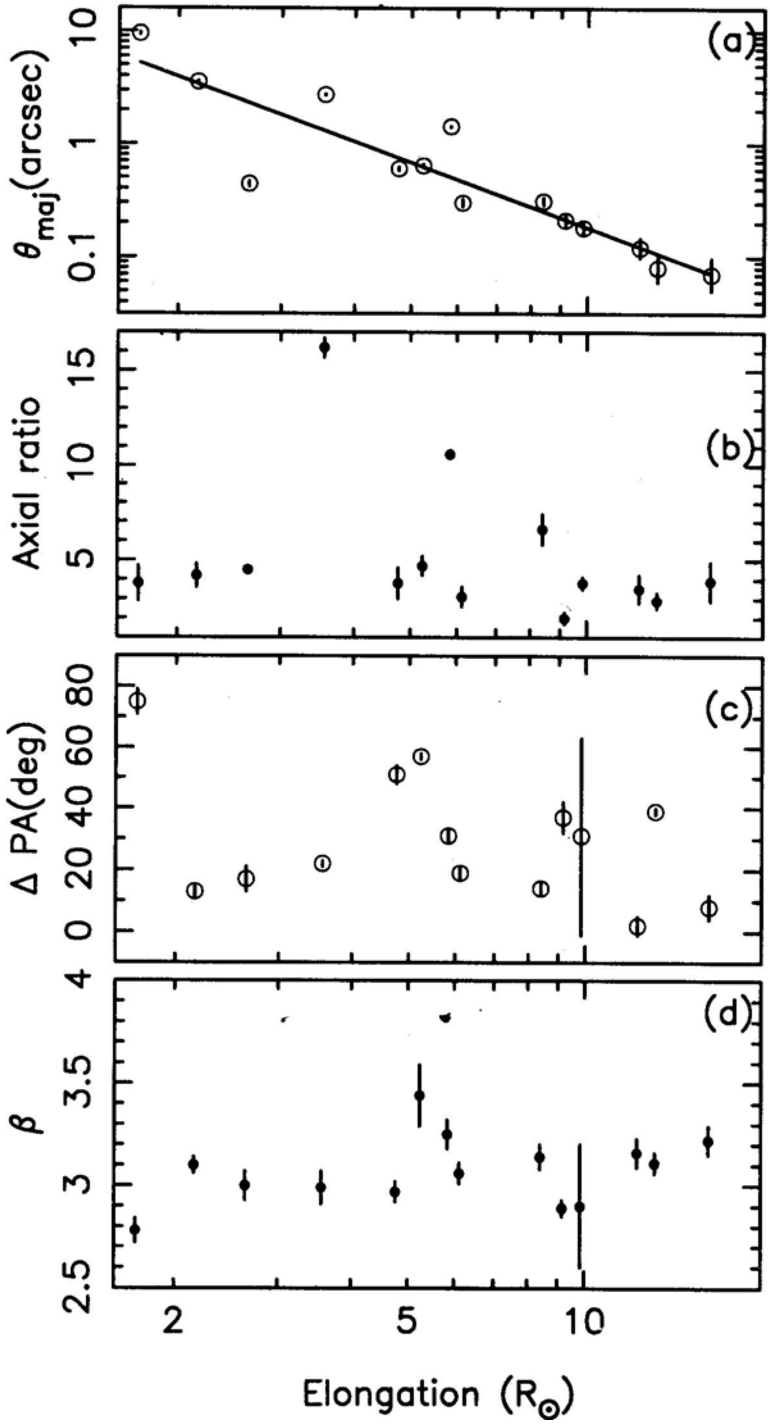

Figure 10. Observed variation of different parameters with solar distance: (a) angular size of the major axis, (b) axis ratio, (c) deviation of position angle of the minor axis from the radial direction and (d) spectral index of the electron density fluctuation spectrum.

maximum when the density fluctuations are expected to be spherically symmetric (Manoharan 1993).

Presence of a transonic region in the solar wind .between 10–20 $R_\odot$ with enhanced scattering properties has been reported by Lotova *et al.* (1985, 1989). It is claimed that in this region, the scattering angles exceed the expected values based on $\theta \propto R^{-1.6}$. In Fig. 10a, there are only 3 data points in the transonic region and they do not show any excess scattering. Further observations are required to confirm the existence of such a region. We note that VLA is well suited to investigate this region using observations at λ = 20 and 90 cm.

5.3 *Anisotropy*

In the elongation range observed here (2–16$R_\odot$), all the scatter-broadened images show anisotropy with the axial ratio ranging from 2 to 16 (Tables 2 and 3). The magnitude of anisotropy does not show any strong dependence on solar distance (Fig. 10b), although larger axial ratios tend to occur only at smaller elongations. Armstrong *et al.* (1990) report marked increase in the axial ratio inside of 6$R_\odot$. However, the difference here is that smaller axial ratios are observed at all elongations and larger axial ratios are observed only at smaller elongations. As seen in Fig. 11a,

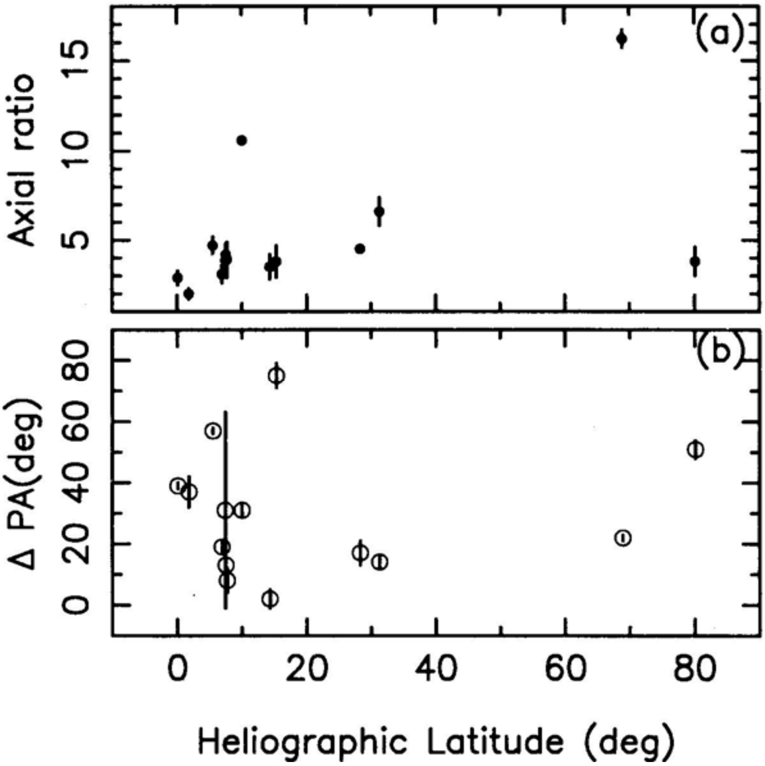

Figure 11. Observed variation of different latitude, of the axial ratio and the deviation of the position angle of the minor axis from radial direction.

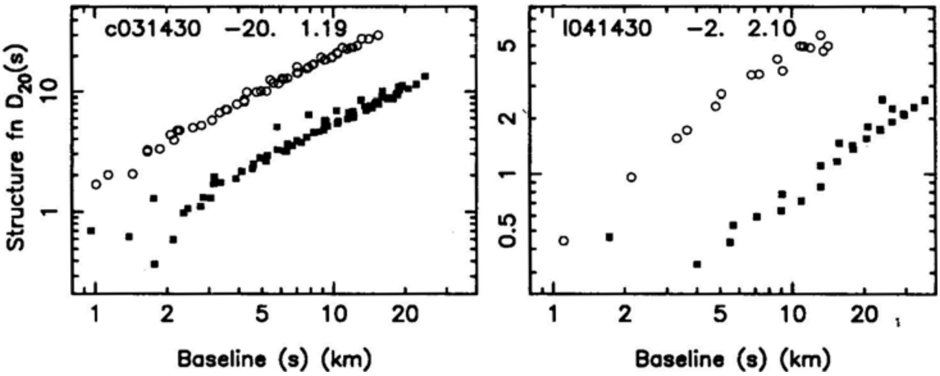

Figure 12. Examples of observe structured function along the major (open circles) and minor (filled squares) axes scaled to $\lambda = 20$ cm. The observed source is 1430–155 at elongations of 1.19°and 2.10°. The position angles of the major axis are – 20° and – 2°.

there could be a dependence of the axial ratio with heliographic latitute; images in the equatorial region seem to show less anisotropy.

Anisotropy in the scattered image implies anisotropy of the scattering blobs which is perhaps caused due to the blobs being ‘stretched’ along magnetic field lines. The amount of this ‘stretching’ may depend on the scale size and the density contrast. It is therefore useful to see whether anisotropy depends on the scale size sampled by these observations (i.e. 1–35 km). In Fig. 12, we show the observed structure functions along the major and minor axis for two of the observations. This figure could be compared with the schematic diagram of Armstrong *et al.* (1990) (their figure 6) which illustrates the expected behaviour when the medium is anisotropic on all scales and when the medium is isotropic near the inner scale. The structure functions in Fig. 12 do not show any inner scale down to 1–2 km and therefore these observations cannot determine whether the inner scale is isotropic or anisotropic. Note that the scatter seen near the shortest baselines in Fig. 12, especially along the minor axis, is due to the source being unresolved and cannot be interpreted as any break in the slope which is expected near the inner scale. Since the structure functions along the major and minor axis, shown in Fig. 12, are essentially parallel to each other in the baseline range 2–35 km, we conclude that the anisotropy is constant over this range of scales.

5.4 *Orientation of the magnetic field lines*

The position angle of the minor axis of the scatter-broadening image indicates the direction along which the scattering blobs are stretched and therefore the local orientation of the magnetic field lines. In Fig. 13, we show the observed position angle of the minor axis at various solar distances. Consistency between the position angles derived from image and visibility analysis indicates that the values are reliable. It is clear that the field lines deviate significantly from the radial direction in many of the positions observed. In contrast, Armstrong *et al.* (1990) have observed that the position angles outside of about 2.5 $R_\odot$ is essentially radial. The difference could be due to our observations being closer to a solar maximum. The observed deviation does not have any strong dependence on radial distance (Fig. 10c) or heliographic latitude (Fig. lib). When the kinetic energy density exceeds the magnetic energy density, one expects the field lines to be radial. The present data implies that, during solar maximum, the magnetic energy density could be comparable to the kinetic energy density even beyond $10R_\odot$.

5.5 *Spectrum of density fluctuations and the inner scale*

On the assumption that the electron density fluctuations in the solar wind has a power law spectrum of the form $P_{Ne}(q) \propto q^{-\beta}$ for $q_{\text{out}} < q < q_{\text{in}}$, where q is the wavenumber, the derived value of the spectral index β is in the range 2.8 to 3.4 with a mean of 3.1 (Tables 2 and 3) which is significantly small compared to the Kolomogorov value of 3.67. No dependence of β is seen either with radial distance from the Sun (Fig. 10d) or heliographic latitude. This value of the exponent applies to scale sizes in the range 2–35 km corresponding to the interferometer baselines used and is consistent with the values obtained by Coles & Harmon (1989) and Manoharan *et al.* (1994) for similar scale sizes using other methods. We have carefully examined the structure function plots (see Fig. 4) for all the sources for baselines along the three arms of the VLA and also along the major and minor axis of the scatter broadened image. We find no instance of any significant change in the value of the exponent with position angles. In most cases the structure function is well sampled in the range 3–30 km and could generally be fitted with a single slope with a value between 0.8 and 1.4.

Upper limits to the inner scale obtained by examining the structure function plots at various solar distances (Fig. 6) are given in column 11 of Table 3. The upper limits range from 1.5 km at 1.7 $R_\odot$ to about 4km at 13 $R_\odot$. The upper limits to the inner scale at solar distances 8–16 $R_\odot$ are more than a factor of two smaller than the inner scale values estimated by Coles & Harmon (1989) using spectral broadening data taken in 1984. If this difference is real, then we could speculate that the inner scales are smaller during a solar maximum.

It is clear that structure function plots such ass presented in Figs. 6 and 12, which can be obtained from interferometric observations are very useful in determining the

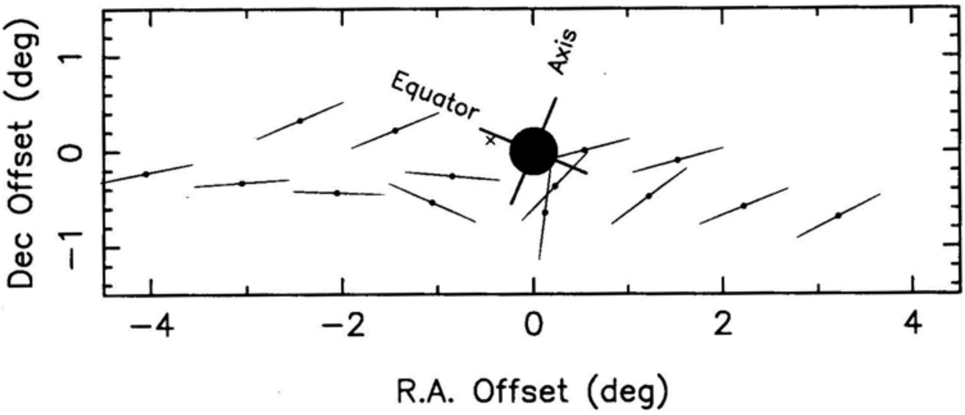

Figure 13. Orientation of the minor axis of scatter-broadened images at the observed positions. The axis of Sun's rotation and the equatorial plane are also indicated.

spectrum of density fluctuations as well as the inner scale. The multiple operating wavelengths of the VLA has been especially useful in selecting the data at the right wavelength to get a well determined structure function at a given solar distance. It would be useful to know, before hand, the right wavelength to choose for the observations if one is interested in making useful structure function measurement at a given scale (i.e. baseline) and a given solar distance. As discussed earlier, useful measurements can be made only if the scatter-broadened source is just or partially resolved by the baselines of interest. Since the angular size of the broadened source (θ_S) scales as λ^2 and the resolution on a given baseline (θ_b) scales as λ/s, the right wavelength of observation at which $\frac{\theta_s}{\theta_b} \sim 1$ is given by $\lambda_{\mathrm{obs}} = \lambda_0^2/s\theta_0$ Here θ_0 is the observed angular size at a wavelength λ_0. Using the measured angular size given in column 5 of Table 3 and the power-law fit to θ_{maj} versus solar distance R in Fig. 10a, we get an empirical relation $\lambda_{\mathrm{obs}} \simeq 4.5\frac{R^{1.6}}{s}$, where R is expressed in units of $R_\odot$.

This gives the preferred observing wavelength (within a factor of 1.5), for an interferometric array with baselines ~ s, to make useful structure function measurements at a solar distance R over scale sizes of the order of s.

Acknowledgements

We thank A. Pramesh Rao, R. Narayan, B. J. Rickett and P. K. Manoharan for many illuminating discussions and the referee W. A. Coles whose critical comments and corrections have significantly improved the contents of this paper. The Very Large Array is a part of NRAO which is operated by Associated Universities Inc. under a cooperative agreement with the NSF.

References

Armstrong, J. W., Coles, W. A., Kojima, M., Rickett, B. J. 1986, in *The Sun and the Heliosphere in Three Dimensions*, Ed. R. G. Marsden (Dordrecht: Reidel) p. 59.
Armstrong, J. W., Coles, W. A., Kojima, M., Rickett, B. J. 1990, *Astrophys. J.*, **358**, 692.
Blesing, R. G.,Dennison, P. A.1972, *Proc. Astr. Soc. Aust.*, **2**, 84.
Coles, W. A., Harmon, J. K. 1989, *Astrophys. J.*, **337**, 102.
Cornwell,T. J., Fomalont, E. B. 1989, in *Synthesis Imaging inRadio Astronomy*, Ed. R.A.Perley, F. R. Schwab & A. H. Bridle, ASP (San Francisco: ASP), p. 185
Cornwell, T. J., Anantharamaiah, K. R., Narayan, R. 1989, *J. Opt. Soc. Am. A*, **6**, 977.
Cronyn, W. M. 1972, *Astrophys. J.*, **174**, 181.
Erickson, W. C. 1964, *Astrophys. J.*, **139**, 1290.
Goodman, J., Narayan, R. 1989, *Mon. Not. R. astr. Soc*, **238**, 995.
Hewish, A. 1955, *Proc. R.Soc.*, **228**, 238.
Hewish, A. 1958, *Mon. Not. R. astr. Soc.*, **118**, 534.
Hewish, A, Scott, P. F, Wills, D. 1964, *Nature*, **203**, 1214.
Hogbom, J. A. 1960, *Mon. Not. R. astr. Soc.*, **120**, 530.
Hollweg, J. V. 1970, *J. Geophys. Res.*, *Space Phys.*,**75**, 3715.
Lotova, N. A., Blums, D. F., Vladimirski, K. V. 1985, *Astr. Astrophys.*, **150**, 266.
Lotova, N. A., Medvedeva, O. P., Kazimirskii, P. B., Sololeva, N. S., Naugol'naya, M. N. 1989, *Soviet Astr.*, **33**, 333.
Machin, K. E., Smith, F. G. 1952, *Nature*, **170**, 319.

Manoharan, P. K. 1993, *Solar Phys.*, **148**, 153.
Manoharan, P. K., Kojima, M., Misawa, H. 1994, *J. Geophys. Res.*, (in press).
Narayan, R., Goodman, J. 1989, *Mon. Not. R.astr. Soc.*, **238**, 963.
Narayan, R., Hubbard, W. B. 1987, *Astrophys. J.*, **325**, 503.
Narayan, R., Anantharamaiah, K. R., Cornwell, T. J. 1989, *Mon. Not. R. astr. Soc.*, **241**, 403.
Narayan, R., Cornwell, T. J., Goodman, J., Anantharamaiah, K. R. 1990, in *Radio Astronomical Seeing*, Ed. J. E. Baldwin & W. Shouguan, (Beijing: International Academic Press).
Slee, O. B. 1959, *Aust. J. Phys.*, **12**, No. 2.
Vitkevich, V. V. 1955, *Doklady Akad. N auk SSSR.*, **101**, 42.